Evolution of infragravity waves over a shoal under non-breaking conditions

Li Shaowu (Orcid ID: 0000-0002-5633-9201)

Liao Zhiling (Orcid ID: 0000-0002-2577-3822)

Liu Ye (Orcid ID: 0000-0001-8993-7315)

Zou Qingping (Orcid ID: 0000-0002-5332-0855)

Evolution of infragravity waves over a shoal under non-breaking conditions

Shaowu Li[1], Zhiling Liao[1], Ye Liu[1, 2], and Qingping Zou[3]

[1] State Key Laboratory of Hydraulic Engineering Simulation and Safety, Tianjin University, Tianjin, China.

[2] Tianjin Research Institute for Water Transport Engineering, M.O.T., Tianjin, China.

[3] The Lyell Centre, Institute for Infrastructure and Environment, Heriot-Watt University, Edinburg, UK.

Corresponding author: Ye Liu (liuye2009@tju.edu.cn)

Key Points:

- Wave history has significant effects on the subsequent evolution of infragravity waves.
- Infragravity wave energy is significantly amplified by a near shore shoal.
- Short waves continually transfer energy to infragravity waves when propagating across the shoal.

This article has been accepted for publication and undergone full peer review but has not been through the copyediting, typesetting, pagination and proofreading process which may lead to differences between this version and the Version of Record. Please cite this article as doi: 10.1029/2019JC015864

Abstract

The present paper aims to clarify the mechanism of infragravity wave (IGW) energy amplification over nearshore shoals reported in recent studies. Wave transformation and energy transfer between short waves (SWs) and IGWs were investigated using SWASH model for non-breaking random waves propagating over trapezoid shoals with different bottom slopes. It was found that the time lag of IGWs relative to SW groups is the major mechanism for energy transfer from SWs to IGWs and the amplification of IGW energy over all segments of the shoal. The time lag is generated on the front slope and enlarged on the plateau of the shoal, decreases on the rear slope at the rate that is higher on milder slopes. Over the rear slope, the evolution of IGWs depends on the relative importance of de-shoaling and nonlinear energy transfer. It was found that nonlinear energy transfer dominates over the rear slope gentler than 1/60, causing the IGW energy to increase over the first half of the de-shoaling process and decrease over the second half whereas de-shoaling dominates for larger rear slope and the IGW energy decay over the whole slope. It is demonstrated numerically and theoretically that the shoals with gentler bottom slopes amplify the IGW energy more effectively by providing longer distance for nonlinear energy transfer to build up. The persistent nonlinear energy transfer on the plateau indicates the important role of wave history in the IGWs evolution when SWs propagate over uneven bottoms. Strong free IGWs were detected on leeward of the shoal, possibly due to release of topography-induced additional bound IGWs.

1. Introduction

Infragravity waves (IGWs) are waves with frequencies remarkably lower than short waves (SWs), typically between 0.004 and 0.04 Hz. *Munk* [1949] and *Tucker* [1950] are the pioneers in recognizing such a low-frequency motion outside the surf zone from field observations and termed it as 'surf beat'. Since then, the important contributions of IGWs have been recognized in many aspects of coastal hydrodynamics and engineering problems, such as resonance in harbor [*Maa et al.*, 2010; *Okihiro et al.*, 1993; *Thotagamuwage and Pattiaratchi*, 2014b], beach and dune erosion [*Roelvink et al.*, 2009], nearshore sediment transport [*De Bakker et al.*, 2016a], and short-wave groupiness on coral reef flat [*Liu and Li*, 2018]. The bound long wave theory of *Longuet-Higgins and Stewart* [1962] (hereinafter referred to as LHS62) suggests that the nonlinear subharmonic waves in equilibrium with the wave group is a key mechanism of IGWs generation. This theory has been widely verified by field observations [*Elgar et al.*, 1992; *Masselink*, 1995], numerical studies [*List*, 1992; *Van Dongeren et al.*, 2002] and laboratory investigations [*Baldock et al.*, 2000; *Kostense*, 1984].

Over the last decades, evolution of IGWs on sloping beaches has attracted more and more attentions. In the shoaling zone, equilibrium between bound IGWs and wave group cannot be maintained so that the biphase of primary SWs and bound IGWs becomes smaller than π [*De Bakker et al.*, 2015; *De Bakker et al.*, 2016b; *Herbers et al.*, 2000] , therefore, nonlinear energy transfer from SWs to IGWs [*Eldeberky and Battjes*, 1995; *Herbers and Burton*, 1997]. The deviation of biphase from π represents a time lag of the bound IGWs with respect to the SW

group, which has been reported by many researches [*Battjes et al.*, 2004; *De Bakker et al.*, 2013; *Inch et al.*, 2017; *List*, 1992; *Masselink*, 1995]. *Bowers* [1992] and *Van Leeuwen* [1992] found that an additional bound IGW is generated over a bottom slope and the time lag of IGWs to SW is generated by the perturbation to the equilibrium solution on flat bottom by water depth variation. This additional bound IGW is in quadrature with and superposed on the bound IGW predicted by the equilibrium solution on a flat bottom (LHS62) and causes a phase shift of the latter.

IGWs can also be generated when wave groups propagate over uneven bottoms in intermediate water depths [*Chu and Mei*, 2006; *Liu*, 1989; *Mei and Benmoussa*, 1984; *Molin*, 1982]. Latter, *Zou* [2011] derived an analytical solution of IGWs over a topography with finite and variable depth based on the linearized shallow-water equation with a forcing term related to wave radiation stress using a multiphase Wentzel–Kramers–Brillouin method. It was reported that an additional bound IGW is generated by the variable depth, which is in quadrature with its uniform-depth counterpart and causes nonlinear energy transfer.

Recently, Paniagua-Arroyave et al. (2019) reported that an isolated shoal with gentle slopes on both sides (Shoal E in Figure 1) is a potential source of IGW energy flux when the direction of incident wave is normal to the orientation of the shoal. The shoal has a gentle front slope of around 1/167 and a shoreward rear slope of around 1/400. For shoreward-propagating SWs, the observed energy fluxes of IGWs at the inner swale (rear slope) of the shoal are much larger than that at the outer swale (front slope), even though the water depths at both swales were nearly the same (Figure 2E). However, no further detailed investigation on this issue was conducted.

Another example is the Chengmai Bay in Hainan Province, China, where the mooring condition of a harbor basin is worsened by an underwater shoal located in the bay mouth roughly parallel to the coastline. *Li et al.* [2018] found from numerical simulations that the IGW energy is greatly enhanced after propagating across the shoal, which may account for the observed substantial long period oscillations in the harbor. IGW energy growth and harbor resonance, independent of the offshore wave conditions, was also observed in Two Rocks Marina of Australia with an offshore-submerged reef system [*Thotagamuwage and Pattiaratchi*, 2014a]. Unlike waves propagating over a straight sloping beach, waves propagating over a shoal undergo changes from shoaling to de-shoaling. However, up to now most of the literatures in the past decades focused on wave evolutions in the shoaling and surf zones (see the comprehensive review of *Bertin et al.* [2018]) with little attention to the de-shoaling zone.

In this study, the evolutions of SWs and IGWs across a typical shoal of various slopes were investigated using the nonhydrostatic wave model SWASH (Simulating WAves till SHore) [*Zijlema et al.*, 2011]. The bispectral analysis was used to quantify the energy exchange between IGWs and SWs. In particular, contributions of nonlinear triad interactions to the IGW energy evolution on the plateau, and combined effects of nonlinear triad interaction and de-

shoaling on the rear slope of the shoal were investigated. The paper is organized as follows: Section 2 introduces the SWASH model, model set-up, and detailed descriptions of the analysis methods; The energy transfer among wave components of different frequencies, energy balance and phase relationship between IGWs and SWs under the influences of bottom slope are illustrated in Section 3; Section 4 discusses the cumulative effects of nonlinear energy transfer, the role of wave history on the nonlinear wave evolution and the composition of IGWs behind the shoal. Conclusions are given in Section 5.

2. Methodology

2.1. Numerical experiment

2.1.1. Numerical model

The multilayer non-hydrostatic model SWASH was used to calculate the time series of water surface elevations in the computational domain. The 2-D governing equations are the momentum and mass conservation equations

$$\frac{\partial u}{\partial t}+\frac{\partial uu}{\partial x}+\frac{\partial wu}{\partial z}=-\frac{1}{\rho}\frac{\partial\left(p_h+p_{nh}\right)}{\partial x}+\frac{\partial \tau_{xz}}{\partial z}+\frac{\partial \tau_{xx}}{\partial x} \tag{1}$$

$$\frac{\partial w}{\partial t}+\frac{\partial uw}{\partial x}+\frac{\partial ww}{\partial z}=-\frac{1}{\rho}\frac{\partial p_{nh}}{\partial z}+\frac{\partial \tau_{zz}}{\partial z}+\frac{\partial \tau_{zx}}{\partial x} \tag{2}$$

$$\frac{\partial u}{\partial x}+\frac{\partial w}{\partial z}=0 \tag{3}$$

where t denotes the time, x and z are the horizontal and vertical coordinates, $u(x, z, t)$ and $w(x, z, t)$ are the horizontal and vertical velocities, g is the gravitational acceleration, p_h is the hydrostatic pressure, p_{nh} is the non-hydrostatic pressure, τ is the turbulent stress described by the standard k-ε model [*Launder and Spalding*, 1974].

The SWASH model is essentially a RANS equation solver capable to describe the processes of wave motion with strong nonlinearity [*Kirby*, 2017]. The model has been extensively validated against both laboratory [*De Bakker et al.*, 2016b] and field data [*Rijnsdorp et al.*, 2015] of nearshore wave evolution with strong nonlinearity. Detailed descriptions of the model can be found in the *Rijnsdorp et al.* (2014) and *Smit et al.*, (2014).

2.1.2. Model set-up

The numerical test runs were conducted in a 2-D vertical numerical wave flume with an efficient computational domain of 160 m long (Figure 3). A series of isosceles trapezoidal shoal with four different slopes of 1/100, 1/80, 1/60 and 1/40 (See Figure 3 and Table 1) were placed

in the middle of the flume. In all cases, the top of the shoal was fixed between 70 m $\leq x \leq$ 90 m at a water depth of 0.3 m, which was slightly deeper than the critical water depth of wave breaking, and the bottom of the shoal is at a water depth of 0.85 m.

The incident significant wave height and peak period for all test cases were 0.1 m and 2.25 s. The enhancement factor γ of the incident JONSWAP spectrum was set to 20 to obtain a relatively narrow band condition. The wave conditions in the present study are identical to that of Run A3 in the experiment of the GLOBEX project for an energetic swell [*Ruessink et al.*, 2013] in the nearshore region to drive a typical pattern of IGWs evolution.

At the inlet boundary on the left side of the flume, a second order wave theory was prescribed to suppress the generation of spurious free IGWs, and a weakly reflective condition was adopted to prevent re-reflections [*Rijnsdorp et al.*, 2014]. A Sommerfeld condition, in combination with a 20 m long sponge layer (not shown in Figure 3), was used to absorb the outgoing waves at the outlet boundary on the right side of the domain. Same time series of incident waves was specified for all the tests.

Six layers were adopted in the vertical direction to ensure the accuracies of dispersion and nonlinearity in the simulations according to *Smit et al.* [2014] and *De Bakker et al.* [2016b]. Water surface elevations were sampled at a frequency of 10 Hz at each grid point. Following *De Bakker et al.* [2016b], the horizontal grid size and computational time step of 0.02 m and 0.002 s were selected. Each model run lasts 65 min, including a 5 min warming-up. Since the present study focuses on the energy transfer due to nonlinear triad interaction, the bottom friction that may complicate the analysis, therefore, is ignored by adopting a zero friction factor.

2.2. Analysis methods

2.2.1. Reflected waves from front slope

Over the front slope, seaward−propagating IGWs may occur due to reflection. However, it is generally difficult to separate them from the incident IGWs. Wave reflection at an underwater bathymetry like a shoal is much smaller than that at a natural emerging shore [*Dong et al.*, 2009]. Additionally, as shown in Section 4.3, the IGW elevation at wave-maker boundary is perfectly matched with the second-order theoretical prediction, suggesting a negligible reflection from the shoal. Considering that the main purpose of the present study was the amplification of IGW energy by the shoal, decomposition of incident and seaward−propagating IGWs was not performed.

2.2.2. Critical frequency between SWs and IGWs

SWs and IGWs can be clearly discriminated in the frequency domain. The filtering frequency between them is usually set to be half of the peak frequency $f_p/2$ of SWs in previous studies [*Liu and Li*, 2018; *Mase*, 1989; *Roelvink and Stive*, 1989; *Sheremet et al.*, 2011]. The adoption of this frequency is reasonable because for a unimodal wave spectrum in deep water, the energy

at frequencies lower than $f_p/2$ is negligible. Alternatively, *De Bakker et al.* [2015], by observing the wave spectra near the wave-maker, adopted a frequency where the wave spectrum is minimum. In the present study, both approaches were tested beforehand and little difference between them was found. Therefore, the frequency $f_p/2$ (0.22 Hz) was adopted in the following sections. The SW energy, E_{SW}, and the IGW energy, E_{IGW}, are obtained in the corresponding frequency bands.

2.2.3. Cross-correlation analysis

The time lag between IGWs and SW group, which relates to energy transfer between SWs and IGWs, was evaluated using a cross-correlation function between IGWs and SW group envelope. The concept of wave height history (*WHH*), proposed by *Liu and Li* [2018], was used to derive the SW group envelope. The *WHH* is defined as

$$WHH(t) = H_n \qquad t_n \le t < t_{n+1} \tag{4}$$

where H_n is the wave height of the n-th wave determined from zero-downcrossing method and t_n the time of the n-th zero-downcrossing point. Once the IGWs signal $\eta_{IG}(x, t)$ and the $WHH(x, t)$ were determined, the correlation between them was given by

$$COR_{\eta_{IGW},WHH}(x,\tau) = \frac{\overline{\eta_{IGW}(x,t)\cdot WHH(x,t+\tau)}}{\sigma_{\eta_{IGW}}\sigma_{WHH}} \tag{5}$$

where τ denotes the time delay between $\eta_{IGW}(x, t)$ and $WHH(x, t)$ and the overbar denotes the time averaging operator. $\sigma_{\eta_{IGW}}$ and σ_{WHH} are the standard deviations of $\eta_{IGW}(x, t)$ and $WHH(x, t)$, respectively.

2.2.4. Bispectral analysis and nonlinear energy transfer

Since introduced by *Hasselmann et al.* [1963], bispectral analysis has been applied widely to study the nonlinear processes of waves, including breaking, shoaling and nearshore dissipation of IGWs [*De Bakker et al.*, 2015; *De Bakker et al.*, 2016b; *Eldeberky and Battjes*, 1995; *Elgar*, 1989; *Herbers and Burton*, 1997; *Herbers et al.*, 2000].

Given a discrete time-series of signal with finite length, the discrete bispectrum is defined as

$$B_{f_1,f_2} = \mathbf{E}\left[A_{f_1}A_{f_2}A^*_{f_1+f_2}\right] \tag{6}$$

where $\mathbf{E}[\bullet]$ is the ensemble average of the triple product, A is the complex Fourier coefficients of the signal and the asterisk denotes complex conjugation.

The normalized magnitude of the bispectrum $b^2_{f_1,f_2}$, referred to as bicoherence, provides a measure of coupling intensity. It is defined as

$$b^2_{f_1,f_2} = \frac{\left|B_{f_1,f_2}\right|^2}{P_{f_1}P_{f_2}P_{f_1+f_2}} \tag{7}$$

where P denotes the power at frequencies f_1, f_2, and their sum $f_1+ f_2$.

In this study, each time series of wave was separated into 4 segments of 15 min long in order to diminish the variance. Averaging the bispectrum over 15 frequencies resulted in a frequency resolution of 0.0167 Hz and 240 degrees of freedom. The estimated bispectrum was accepted at a confidence level of 95%.

The phase of the bispectrum β_{f_1,f_2}, referred to as biphase, represents the phase relationship among the associated wave components and is defined as

$$\beta_{f_1,f_2} = \mathrm{Arg}\left(B_{f_1,f_2}\right) \tag{8}$$

where Arg(•) denotes the principal value of the argument function of a complex number.

To obtain a comprehensive biphase $\beta_{\mathrm{IGW,SW}}$ that represents the phase coupling between SWs and IGWs, the biphase was integrated over the intersection frequency band of SWs and IGWs (ZONE III in Fig. 4 of *De Bakker et al.* [2015]) as follows

$$\beta_{\mathrm{IGW,SW}} = \mathrm{Arg}\left(\sum_{f_2=0.22\mathrm{Hz}}^{0.5\,f_N}\sum_{f_1=0}^{0.22\mathrm{Hz}} B_{f_1,f_2}\right) \tag{9}$$

where f_N = 5 Hz is the Nyquist frequency.

The formula for calculating irregular wave energy evolution in the weakly dispersive regime was proposed by *Herbers and Burton* [1997] based on the Boussinesq theory as

$$\frac{dP_f}{dx} = R_{sh} + R_{nl} = -\frac{1}{2h}\frac{dh}{dx}P_f + \frac{3\pi f}{h\sqrt{gh}}\sum_{f'=-\infty}^{+\infty} IM\left(B_{f',f-f'}\right) \tag{10}$$

where h is the water depth, IM(•) denotes the imaginary part of a complex number. The first term on the *right hand side* of Eq. (10), R_{sh}, represents the linear shoaling term and the second term, R_{nl}, is the contribution of nonlinear triad interactions. The direction of nonlinear energy transfer is determined by the sign of the bispectrum imaginary part. A negative imaginary part indicates an energy transfer from the sum frequency $f_3 = f_1+f_2$ to f_1 and f_2 and vice versa.

3. Model results

3.1. Evolution of wave energy

Figure 4a shows the evolution of normalized SW energy over a trapezoid shoal with slope of 1/80 (Run 2). The SW energy increases over the front slope (26 m ≤ x ≤ 70 m) due to shoaling, and then hardly change over the horizontal plateau. At the rear end of the plateau, wave

reflection occurs and causes a slight fluctuation of the SW energy. During de-shoaling on the rear slope, the SW energy decreases at a faster rate than the rate of increase in SW energy while shoaling over the front slope, and achieves approximately 10% increment in total at the end of the rear slope. Figure 4b shows the cross-shoal evolution of normalized IGW energy. The IGW energy increases throughout the front slope and continue so over the plateau at a constant rate despite the uniform depth. On the rear slope, interestingly the IGW energy increases slowly in the first half of the slope and then decrease slowly over the rest of the slope despite the fast decaying SW energy. After propagating across the whole shoal, the IGW energy is amplified by nearly 18 times. It must be stressed that the water depths on two sides of the shoal are the same.

Wave energy evolution at different frequency bands is evident from the wave spectra at different locations of the shoal (Figure 5). A Hanning-window of 200 points wide was used, yielding a frequency resolution of 0.0558 Hz and 100 degrees of freedom. On the front slope (Figure 5a), the wave at superharmonic frequency increases rapidly while the primary wave at the peak frequency remains nearly constant, indicating an drastic amplification of wave nonlinearity during shoaling. The IGW energy increases over the entire frequency range more so at higher frequencies. However, no dominant IGW frequency is observed on the front slope. Over the plateau (Figure 5b), the SW energy at the peak frequency and its superharmonic peaks decreases while the energy between two neighboring peaks increases. The primary wave band becomes wider with distance although the total energy within the band hardly changes (Figure 4a), indicating an energy transfer from the peak to its side bands on either sides. The IGW energy keeps increasing and eventually a subharmonic peak at about 0.04 Hz arises at the end of the plateau. On the rear slope (Figure 5c), the superharmonic peaks vanish and the primary peak becomes insignificant. As a result, the spectrum of the SWs is flattened after propagating across the shoal. Noteworthily, the IGW energy remains almost unchanged on the rear slope despite of the de-shoaling effect and weakened SW.

3.2. Nonlinear wave energy transfer

Figure 6 shows the imaginary parts of the bispectra in a frequency-frequency plot for waves at different locations across the shoal. At the initial stage of shoaling (Figure 6a), the bispectral imaginary parts exhibit negative values at (0.44, 0.44) Hz and alternating positive and negative values in its vicinity, suggesting an energy exchange between superharmonics and primary harmonics. The weakly negative values around (0.43, 0.01) Hz suggest an energy transfer from the peak frequency 0.44 Hz to 0.01 Hz and their difference frequency 0.43 Hz. As waves advance on the front slope, positive values dominate around (0.44, 0.44) Hz, indicating a strong energy transfer to the first harmonic at 0.88 Hz. Meanwhile, the negative value area spreads and its values grow in magnitude as well (Figure 6a-c), indicating the energy transfer intensity grows with distance.

On the plateau (Figure 6d), negative values concentrate on (0.40, 0.04) Hz, indicating an energy transfer from the primary peak frequency 0.44 Hz to 0.40 Hz and the subharmonic peak 0.04

Hz. On the rear slope (Figure 6e and f), the negative value area shifts further leftward while its vertical coordinate keeps constant, implying that the subharmonic peak is basically fixed while the primary peak frequency gradually decreases. Figure 7 presents a quantitative analysis of the nonlinear energy transfer between SWs and IGWs, in which the shoaling term $R_{IG,sh}$ and the nonlinear interaction term $R_{IG,nl}$ of the IGW energy on the *right hand side* of Eq. (10) were obtained by applying Eq. (10) to each component of the IGWs and then integrating over the infragravity frequency band (0-0.22 Hz) as shown below,

$$R_{IG,sh} = \sum_{f=0}^{0.22\text{Hz}} \left(-\frac{1}{2h}\frac{dh}{dx} P_f \right), \tag{11}$$

$$R_{IG,nl} = \sum_{f=0}^{0.22\text{Hz}} \left[\frac{3\pi f}{h\sqrt{gh}} \sum_{f'=-\infty}^{f} IM\left(B_{f,f-f'}\right) \right]. \tag{12}$$

Gradient of the IGW energy was obtained through linear regression of the simulated IGW energy over twice the peak wavelength. Figure 7a shows a good agreement between the sum of source terms ($R_{IG,sh}$+$R_{IG,nl}$) and the linear regression. Cross-shoal variations of $R_{IG,sh}$ and $R_{IG,nl}$ in Figure 7b indicates that $R_{IG,sh}$ follows the gradient of the water depth, keeps positive and increases over the front slope, decays to zero over the plateau and then becomes negative over the rear slope. Meanwhile, $R_{IG,nl}$ remains positive across the shoal, implying that the IGWs gain energy from the SWs through nonlinear interactions, which is the mechanism for the amplification of IGW energy, as indicated in Figure 4b. $R_{IG,sh}$ and $R_{IG,nl}$ have the same sign over the front slope but opposite signs over the rear slope with comparative magnitudes. The constructive sum leads to the fast growth of IGW energy over the front slope while the counteraction of the nonlinear energy transfer and de-shoaling effects causes slow variation over the rear slope.

3.3. Phase relationship between waves

As stated in the introduction section, the biphase of SWs and bound IGWs becomes smaller than π in the shoaling process implying a time lag of the IGWs behind the group envelope. The deviation of biphase from π represents the unbalanced nonlinear coupling between bound IGWs and SWs, therefore nonlinear energy transfer.

The time lag and the biphase $\beta_{IGW,SW}$ develop gradually over the front slope, keep increasing over the plateau and in the early stage of de-shoaling and then start dropping down over the rear slope (Figure 8). At the toe of the rear slope, the time lag resumes zero immediately whereas $\beta_{IGW,SW}$ remains sizable magnitude over a significant distance after the shoal. When waves cease shoaling while entering the plateau, the time lag remains positive, causing the subsequent strong nonlinear energy transfer from SWs to IGWs. According to Figure 7.

b, the nonlinear energy transfer attains the maximum over the plateau, whereas the time lag attains the maximum over the rear slope. The mismatch is because the nonlinear energy transfer magnitude depends not only on the time lag, but also on the SWs amplitudes. By the time the time lag achieves maximum over the rear slope, the SW energy has decayed considerably due to de-shoaling.

The development of time lag on the front slope is attributed to the slowing-down of the IGWs [*Janssen et al.*, 2003]. This phenomenon may be related to the topography-induced additional bound wave which is in quadrature with its flat-bottom counterpart. The superposition of the additional long wave with its flat-bottom counterpart introduces a phase shift to the latter as theoretically demonstrated by *Bowers* [1992], *Van Leeuwen* [1992] and *Zou* [2011]. Over the rear slope, however, the time lag decreases and resumes zero by the end of the slope, indicating that the IGWs speed up and catch up with the SW wave group. This might reflect the fact that the topography-induced additional bound long wave is released gradually over the rear slope. This point will be further discussed in Section 4.3.

3.4. Influence of bottom slope

From the growth rates of IGW energy of all test runs (Figure 9a), it is evident that the IGW energy achieves greater amplification on milder bottom slopes during shoaling. The IGW energy grows at almost same rate over the plateau for different front slopes (Figure 9b). Over the rear slope, however, the IGW energy evolves slightly differently (Figure 9c) over different bottom slopes. The IGW energy slightly decrease all the way over the 1/40 rear slope, whereas it first increases and then decreases over the 1/100 rear slope. As illustrated in Figure 7, the IGW evolution over the rear slope depends on the relative importance of de-shoaling and nonlinear energy transfer. The decreased IGW energy over the 1/40 rear slope indicates that the de-shoaling effect dominates, whereas the increased IGW energy over the 1/100 rear slope implies that the nonlinear energy transfer from SWs to IGWs dominates. When these two factors are about in balance over a 1/60 bottom slope, the IGW energy remains roughly the same over the rear slope. In the present model test runs, the IGW energy achieved a maximum and minimum amplification factors of 19.3 and 12 over the slope of 1/100 and 1/40, respectively.

Unlike the evolution of IGW energy, the time lag maintains nearly the same value over different bottom slopes at the end of the front slopes (Figure 10a). Over the front slope, the time lag is far more sensitive to the local water depth than the bottom slope (Figure 10b). Similar results was observed in the laboratory experiments (Fig. 6 in *Liu et al.* [2010]), where random wave evolution over three slopes of 1/20, 1/30, and 1/40 were investigated. This phenomenon explains the correlation between the IGW energy growth rate and the front bottom slope, as will be further discussed in Section 4.1. Over the rear slope, time lags of all test runs decrease all the way after a slight increase in the beginning of de-shoaling, at a faster rate over milder slopes (Figure 10c).

4. Discussion

4.1. Accumulation of nonlinear wave energy transfer

Same as the previous studies [*Battjes et al.*, 2004; *De Bakker et al.*, 2016b; *Van Dongeren et al.*, 2007], a negative correlation between the IGW energy growth rate and the bottom slope of the shoaling zone is observed in the present study (Figure 9a). The mechanism behind this phenomenon, however, is yet fully understood. Next we will demonstrate theoretically that this negative correlation is attributed to the difference in the distances provided for the accumulation of nonlinear energy transfer over different slopes. Figure 11 shows the evolutions of SW and IGW energy as well as the ratio between them along the front slope. The SW energy is independent of the bottom slope (Figure 11a), while the IGW energy is (Figure 11b). The SW energy is two order of magnitude greater than the IGW energy during the whole process of shoaling (Figure 11c), therefore the nonlinear energy transfer from SWs to IGWs has little influence on the evolution of SW energy. As a result, the SW energy can be described as a function of local depth as formulated by the nonlinear wave shoaling theory [*Shuto*, 1974; *Wang et al.*, 2008].

In summary, the model results in the present study reveals the following facts. Firstly, the nonlinear energy transfer to IGWs has little effect on SWs, therefore under non-breaking conditions, the SW energy and the wave radiation stress mainly depends on the local depth regardless bottom slope. Secondly, over the front slope, the time lag between the IGWs and the SW group envelope is far more sensitive to the local water depth than the bottom slope (Figure 1b). The IGW energy is amplified by the work done by the SW radiation stress on the currents induced by IGW, which is calculated as $-\langle U\frac{dS_{xx}}{dx}\rangle$ [*Phillips*, 1977] given by

$$\frac{dF}{dx}=\frac{1}{2}\hat{U}\left[\kappa\hat{S}_{xx}\sin(\Delta\varphi)+\frac{d\hat{S}_{xx}}{dx}\cos(\Delta\varphi)\right] \tag{13}$$

where F is the IGW energy flux, κ is the wave number of IGW, $\hat{U}$ is the depth-averaged velocity amplitude, $\hat{S}_{xx}$ is the radiation stress amplitude, and $\Delta\varphi$ is the phase difference between IGW and radiation stress. Eq. (13) is identical to Eq. (5.4) in *Zou* [2011], which is expressed in a complex variable form there.

To describe the variation rate of F with water depth, Eq. (13) is rewritten, according to the chain rule, as

$$\frac{dF}{dh}=\frac{dF}{dx}\frac{dx}{dh}=\frac{1}{2}\hat{U}\left[\kappa\hat{S}_{xx}\sin(\Delta\varphi)\frac{dx}{dh}+\frac{d\hat{S}_{xx}}{dh}\cos(\Delta\varphi)\right]. \tag{14}$$

Substituting $F=\frac{1}{2}\rho h c_g\hat{U}^2$, as proposed by *Battjes et al.* [2004], into Eq. (14) yields

$$\frac{dF^{\frac{1}{2}}}{dh} = \frac{1}{\left(8\rho h c_g\right)^{\frac{1}{2}}}\left[\kappa \hat{S}_{xx}\sin(\Delta\varphi)\frac{dx}{dh} + \frac{d\hat{S}_{xx}}{dh}\cos(\Delta\varphi)\right] = RF_{acc} + RF_{sw} \qquad (15)$$

The first term on the *right hand side* of Eq. (15), RF_{acc}, represents the energy growth due to nonlinear energy transfer accumulation and the second term RF_{sw} the energy growth due to the SW radiation stress gradient. All the terms on the *right hand side* of Eq. (15) are independent of the slope except for the factor dx/dh in the term of RF_{acc}. This factor can be interpreted as the distance of SW-IGW interaction with a depth variation. $dx/dh = 1/h_x$ is larger over a milder slope, implying a longer distance for SW-IGW interaction and energy transfer accumulation and therefore a larger IGW energy growth rate.

4.2. Effect of wave history on IGWs

It is interesting to note that energy transfer from SWs to IGWs sustain over the whole plateau that has constant water depth (Figure 9b). This result suggests the effect of wave history over the front slope on the subsequent IGWs evolution afterwards over the plateau, because the theory of LHS62 suggests no energy transfer at the constant water depth over the flat plateau. The subharmonic waves are a function of the primary wave and local spatial derivatives of water depth [*Eldeberky and Battjes*, 1995; *Janssen et al.*, 2003; *Liu et al.*, 2010; Zou, 2010; *Rocha et al.*, 2017]. However, those theories cannot explain the evolution of IGWs at the constant water depth over the flat plateau possibly because those theories do not take the wave shoaling history over the front slope into consideration. Explanation of why wave history on the front slope has substantial influences on the subsequent evolution of the IGW energy on the plateau requires further theoretical investigation. The effects of wave history on the IGW energy evolution were also observed on the rear slope with negative bottom slope. As shown earlier, the non-zero time lag on the plateau triggers the nonlinear energy transfer at the very beginning of de-shoaling over the rear slope.

4.3. Composition of IGWs behind the shoal

Behind the shoal, the IGW energy is considerably amplified while a little drop of the SW energy occurs despite the resume of water depth. The SWs over rear slope of the shoal are no longer capable of driving strong bound IGWs. The nonlinear second-order finite-depth theory of *Hasselmann* [1961] (see Appendix A) can be employed to calculate the bound IGWs that travel over the horizontal bottoms on both sides of the shoal. Taking Run 2 (bottom slope 1/80) as an example, although the bound IGWs dominate the low frequencies of the incident IGWs (Figure12a), the IGW departs significantly from the bound IGW theory (Figure12b). In order to shed some light on this phenomena, an additional simulation was conducted by extending the length of the computational domain (sponge layer not included) from 160 m to 320 m(Figure 13a). In the extended region (160 m $\leq x \leq$ 320 m), the SW energy remains constant, whereas the IGW energy continues to slowly decay all the way (Figure 13b). Result of

bispectral analysis confirms that the energy is slowly transferred from IGWs to SWs in this region (In additon to nonlinear energy transfer, free IGWs were also detected in this region. As shown in Figure 1, in the region of 0 m $\leq x \leq$ 264 m, only one extrema is recognized in the correlation coefficients between the local IGWs and the wave group envelope; in the region of 264 m $\leq x \leq$ 320 m, however, two local extrema are identified in the correlation coefficients, which correspond to two time lags τ_1 and τ_2 ($|\tau_1| < |\tau_2|$). For most of the extended region (160 m $\leq x \leq$ 280 m), the negative τ_1 indicates the energy transfer from IGWs to SWs as shown in Figure 13c. The time lag τ_2 indicates the occurrence of free IGWs propagating at a different speed of $\sqrt{gh}$ from SWs. The release of bound IGWs can explain why the free IGWs are negatively correlated with the group envelope (Figure 14) since the bound IGWs, from which the free IGWs originate, are negatively correlated with the group envelope. Although this explanation seems contradict with the traditional breaking-induced IGWs theory, *Baldock* [2012] argued that the bound IGWs may be released only if they satisfy the same dispersion relationship as free IGWs wave, *i.e.* the shallow-water resonance condition, regardless of wave breaking. They also stated that bound IGWs will be released if SWs propagate in shallow waters prior to breaking. Note that the water depth on the plateau in the present work is close to shallow water for the primary wave ($k_p h$ = 0.51 and $c_g/\sqrt{gh}$ = 0.89, where k_p is the wave number at the peak frequency) as to reach the near-resonance state, the present model results are consistent with the argument of *Baldock* [2012]. This result also highlights the fact that wave breaking is not necessarily the only trigger for the release of bound IGWs.

Comparison among E_{FIGW} of test runs at x = 152 m is illustrated in Figure 15, where E_{FIGW} denotes the free IGW energy and was evaluated by subtracting the theoretical bound IGWs from simulated IGWs. It is evident that E_{FIGW} becomes greater over milder bottom slope. In addition, the free IGWs are far stronger than the bound IGWs for all the slopes. Taking the result of model test Run 4 (bottom slope 1/40) as an example, the significant wave height of free IGWs at x = 152 m is evaluated to be 0.0204 m, whereas that of bound IGWs is 0.0074 m. Note that the wave conditions in the present study follow the laboratory scale counterpart of the GLOBEX experiment [*Ruessink et al.*, 2013]. If transformed to field condition with a geometric scaling factor of 1:20, the significant wave heights of the free IGWs and the bound IGWs would be 0.408 m and 0.148 m, respectively.

5. Conclusions

A series of numerical experiments were conducted using SWASH model to investigate the evolution the IGW energy over a symmetric trapezoidal shoal with different bottom slopes. It was found that the IGW energy can be significantly amplified by the nonlinear energy transfer from SWs to IGWs when SWs propagate over uneven topography at a finite water depth. Without wave breaking, the IGW energy always increases over the front slope and the subsequent plateau, but may increase or decrease over the rear slope, depending on the relative importance of the de-shoaling and nonlinear energy transfer. These two driving factors achieve

a balance over a slope of approximately 1/60 in the present model set-up, resulting in a nearly constant IGW energy over the rear slope. A shoal with milder bottom slope was found to amplify the IGW energy more.

The nonlinear energy transfer from SWs to IGWs can be evaluated based on the time lag between local IGWs and SW group envelope, which increases during shoaling over the front slope, continues to increase over the plateau and during the early stage of de-shoaling over the rear slope. After that, the time lag decays all the way while de-shoaling over the rest of the rear slope as the water depth recovers its original value in front of the shoal. The total reduction in time lag during the de-shoaling over the rear slope is larger over milder slopes due to longer travelling distance. The time lag was found to be largely dependent on the local depth instead of the bottom slope during shoaling. Based on this observation and the fact that the energy transferred from SWs to IGWs is negligible to the SWs energy, theoretically the stronger IGW energy growth rate on milder rear slopes is attributed to the longer traveling distance for the SW-IGW interaction and the accumulation of nonlinear energy transfer over milder slopes.

The wave history has significant effect on the subsequent nonlinear wave evolution as waves passing over a shoal. The nonlinear energy transfer from SWs to IGWs over the plateau of the shoal is directly influenced by the shoaling history over the preceding front slopes. Without the preceding wave history, there would be no time lag between the IGWs and SW group envelop and consequently the nonlinear energy transfer would not occur over the plateau with constant water depth.

Strong free IGWs were detected on the leeward side of the shoal through cross-correlation analysis. The free IGWs may be generated by the release of the additional bound IGWs after propagating across the shoal. The results support the hypothesis that bound IGWs can be released by topographical change without wave breaking. The released free IGWs on leeward of the shoal are stronger for milder slopes. For the wave conditions of present study, these free IGWs have a significant wave height at the order of decimeters in prototype scale, which may have significant impacts on nearshore sediment and pollutant transport and mooring condition in the harbor behind the shoal.

Acknowledgments

This research work is financed by the National Natural Science Foundation of China (Grant No. 51779170), the Innovative Research Groups of the National Natural Science Foundation of China (Grant No. 51321065), and the Central Public-interest Scientific Institution Basal Research Fund (Grant No. TKS200415). The outputs of the numerical model are available on Zenodo.org (DOI: 10.5281/zenodo.3546534).

Appendix A: *Hasselmann's* [1961] solution for bound IGWs

The bound IGWs is calculated based on the weakly-nonlinear second-order finite-depth wave theory of *Hasselmann* [1961]. The subharmonic component forced by two free wave components at frequency f_i and f_j is

$$\eta_{ij} = D_{ij} a_i a_j \cos\left(\psi_i - \psi_j\right) \tag{A16}$$

where a_i and a_j are the amplitudes of the forcing components, ψ_i and ψ_j the phase. The interaction coefficient D_{ij} is given by

$$D_{ij} = -\frac{gk_i k_j}{2\omega_i\omega_j} + \frac{\omega_i^2 - \omega_i\omega_j + \omega_j^2}{2g} - C\frac{g\left(\omega_i - \omega_j\right)}{\omega_i\omega_j\left[gk_{ij}\tanh\left(k_{ij}h\right) - \left(\omega_i - \omega_j\right)^2\right]} \tag{A17}$$

where $\omega=2\pi f$ is the radial frequency and k is the wave number and $k_{ij} = k_i - k_j$ is the wave number of the subharmonic component. The coefficient C is given by

$$C = \left(\omega_i - \omega_j\right)\left(\frac{\omega_i^2\omega_j^2}{g^2} + k_i k_j\right) - \frac{1}{2}\left[\frac{\omega_i k_j^2}{\cosh^2\left(k_j h\right)} - \frac{\omega_j k_i^2}{\cosh^2\left(k_i h\right)}\right] \tag{A18}$$

The measured surface elevation is first decomposed into Fourier components and then the components with frequency $0.5f_p \le f \le 1.5f_p$ is the forcing primary components. Summarize the subharmonics forced by all pairs of the primary components, the surface elevation of the bound IGW is obtained as

$$\eta = \sum_{f_i=0.5f_p}^{1.5f_p} \sum_{f_j=f_{i+1}}^{1.5f_p} \eta_{ij} \tag{A19}$$

References

Baldock, T. E. (2012), Dissipation of incident forced long waves in the surf zone-Implications for the concept of "bound" wave release at short wave breaking, Coastal Engineering, 60(1), 276-285, doi:10.1016/j.coastaleng.2011.11.002.

Baldock, T. E., D. A. Huntley, P. A. D. Bird, T. O'Hare, and G. N. Bullock (2000), Breakpoint generated surf beat induced by bichromatic wave groups, Coastal Engineering, 39(2), 213-242, doi:https://doi.org/10.1016/S0378-3839(99)00061-7.

Battjes, J. A., H. J. Bakkenes, T. T. Janssen, and A. R. van Dongeren (2004), Shoaling of subharmonic gravity waves, Journal of Geophysical Research: Oceans, 109(C2), doi:10.1029/2003jc001863.

Bertin, X., et al. (2018), Infragravity waves: From driving mechanisms to impacts, Earth-Sci. Rev., 177, 774-799, doi:10.1016/j.earscirev.2018.01.002.

Bowers, E. C. (1992), Low frequency waves in intermediate water depths, in 23rd International Conference on Coastal Engineering, edited, American Society of Civil Engineering, Venice,Italy.

Chu, V. H., and C. C. Mei (2006), On slowly-varying Stokes waves, Journal of Fluid Mechanics, 41(4), 873-887, doi:10.1017/S0022112070000988.

De Bakker, A., J. A. Brinkkemper, F. V. D. Steen, M. Tissier, and B. G. Ruessink (2016a), Cross-shore sand transport by infragravity waves as a function of beach steepness, Journal of Geophysical Research, 121(10), 1786-1799.

De Bakker, A., T. H. C. Herbers, P. B. Smit, M. Tissier, and B. G. Reussink (2015), Nonlinear infragravity–wave interactions on a gently sloping laboratory beach, Journal of Physical Oceanography, 45(2), doi:10.1175/JPO-D-14-0186.1.

De Bakker, A., M. Tissier, V. Marieu, N. Sénéchal, A. Ruju, J. Lara, and B. G. Ruessink (2013), Infragravity wave propagation and dissipation on a low-sloping laboratory beach, Proc. Seventh Int. Conf. on Coastal Dynamics, Bordeaux, 443-452.

De Bakker, A., M. Tissier, and B. G. Ruessink (2016b), Beach steepness effects on nonlinear infragravity-wave interactions: A numerical study, Journal of Geophysical Research Oceans, 121(1), 554-570, doi:10.1002/2015JC011268.

Dong, G., X. Ma, M. Perlin, Y. Ma, B. Yu, and G. Wang (2009), Experimental study of long wave generation on sloping bottoms, Coastal Engineering, 56(1), 82-89, doi:10.1016/j.coastaleng.2008.10.002.

Eldeberky, Y., and J. A. Battjes (1995), Parameterization of triad interactions in wave energy models, paper presented at Coastal Dynamics.

Elgar, S. (1989), Bispectra Of Shoaling Ocean Surface Gravity Waves, paper presented at The Workshop on Higher-Order Spectral Analysis.

Elgar, S., T. H. C. Herbers, M. Okihiro, J. Oltman-Shay, and R. T. Guza (1992), Observations of infragravity waves, Journal of Geophysical Research: Oceans, 97(C10), 15573-15577, doi:10.1029/92jc01316.

Hasselmann, K. (1961), On the non-linear energy transfer on a gravity-wave spectrum. Part 1. General Theory, Fluid. Mech., 12, 481-500, doi:10.1017/S0022112062000373.

Hasselmann, K., W. Munk, and G. MacDonald (1963), Bispectra of ocean waves, John Wiley, New York.

Herbers, T., and M. C. Burton (1997), Nonlinear shoaling of directionally spread waves on a beach, Journal of Geophysical Research Oceans, 102(C9), 21101-21114, doi:10.1029/97JC01581.

Herbers, T., N. R. Russnogle, and S. Elgar (2000), Spectral energy balance of breaking waves within the surf zone, Journal of Physical Oceanography, 30(11), 2723-2737, doi:10.1175/1520-0485(2000)030<2723:sebobw>2.0.co;2.

Inch, K., M. Davidson, G. Masselink, and P. Russell (2017), Observations of nearshore infragravity wave dynamics under high energy swell and wind-wave conditions, Continental Shelf Research, 138, 19-31, doi:http://dx.doi.org/10.1016/j.csr.2017.02.010.

Janssen, T. T., J. A. Battjes, and A. R. van Dongeren (2003), Long waves induced by short-wave groups over a sloping bottom, Journal of Geophysical Research: Oceans, 108(C8), doi:10.1029/2002jc001515.

Kirby, J. T. (2017), Recent advances in nearshore wave, circulation, and sediment transport modeling, Journal of Marine Research, 75(3), 263-300, doi:10.1357/002224017821836824.

Kostense, J. K. (1984), Measurements of surf beat and set-down beneath wave groups, paper presented at 19th International conference on Coastal Engineering, American Society of Civil Engineers, Houston, Texas, United States.

Launder, B. E., and D. B. Spalding (1974), The numerical computation of turbulent flows, Computer Methods in Applied Mechanics and Engineering, 3(2), 269-289, doi:https://doi.org/10.1016/0045-7825(74)90029-2.

Li, S., B. Li, Y. Liu, and Z. Liao (2018), Study on infragravity waves over a nearshore shoal, Journal of Waterway and Harbor, 39(06), 643-651.

List, J. H. (1992), A model for the generation of two-dimensional surf beat, Journal of Geophysical Research Oceans, 97(C4), 5623-5635, doi:10.1029/91JC03147.

Liu, P. L.-F. (1989), Note on long waves induced by short-wave groups over a shelf, Journal of Fluid Mechanics, 205(205), 163-170.

Liu, X. A., W. Q. Lin, and P. J. Huang (2010), Laboratory Study of Low-Frequency Waves Induced by Random Gravity Waves on Sloping Beaches, J Waterw Port Coast, 136(3), 127-134, doi:10.1061/(asce)ww.1943-5460.0000035.

Liu, Y., and S. Li (2018), Variation of wave groupiness across a fringing reef, J Waterw Port Coast, 144(6), 14, doi:10.1061/(asce)ww.1943-5460.0000475.

Longuet-Higgins, M. S., and R. W. Stewart (1962), Radiation stress and mass transport in gravity waves with application to 'surf beats', Journal of Fluid Mechanics.

Maa, P. Y., C.-H. Tsai, W.-J. Juang, and H.-M. Tseng (2010), A preliminary study on Typhoon Tim induced resonance at Hualien Harbor, Taiwan, *61*(4), 411-423.

Mase, H. (1989), Groupiness factor and wave height distribution, Journal of Waterway, Port, Coastal, and Ocean Engineering, 115(1), 105-121, doi:doi:10.1061/(ASCE)0733-950X(1989)115:1(105).

Masselink, G. (1995), Group bound long waves as a source of infragravity energy in the surf zone, Continental Shelf Research, 15(13), 1525-1547, doi:https://doi.org/10.1016/0278-4343(95)00037-2.

Mei, C. C., and C. Benmoussa (1984), Long waves induced by short-wave groups over an uneven bottom, Journal of Fluid Mechanics, 139(139), 219-235, doi:10.1017/S0022112084000331.

Molin, B. (1982), On the generation of long-period second order free-waves due to changes in the bottom profile, Pap. Ship. Res. Inst., Tokyo.

Munk, W. (1949), Surf beats, Eos Transactions American Geophysical Union, 30(6), 849–854.

Okihiro, M., R. T. Guza, and R. J. Seymour (1993), Excitation of seiche observed in a small harbor, Journal of Geophysical Research: Oceans, 98(C10), 18201-18211, doi:10.1029/93jc01760.

Paniagua-Arroyave, J. F., P. N. Adams, S. M. Parra, and A. Valle-Levinson (2019), Observations of surface-gravity-wave scattering and dissipation by an isolated shoal related to a cuspate foreland, Continental Shelf Research, 173, 43-55, doi:https://doi.org/10.1016/j.csr.2018.12.004.

Phillips, O. M. (1977), The Dynamics of the Upper Ocean, 2nd ed., Cambridge Univ. Press, New York.

Rijnsdorp, D. P., G. Ruessink, and M. Zijlema (2015), Infragravity-wave dynamics in a barred coastal region, a numerical study, Journal of Geophysical Research Oceans, 120(6), 4068-4089, doi:10.1002/2014JC010450.

Rijnsdorp, D. P., P. Smit, and M. Zijlema (2014), Non-hydrostatic modeling of infragravity waves under laboratory conditions, Coastal Engineering.

Rocha, M., H. Michallet, and P. A. Silva (2017), Improving the parameterization of wave nonlinearities – The importance of wave steepness, spectral bandwidth and beach slope, Coastal Engineering, 121, 77-89.

Roelvink, D., A. Reniers, A. R. van Dongeren, J. van Thiel de Vries, R. McCall, and J. Lescinski (2009), Modelling storm impacts on beaches, dunes and barrier islands, Coastal Engineering, 56(11), 1133-1152, doi:https://doi.org/10.1016/j.coastaleng.2009.08.006.

Roelvink, J. A., and M. J. F. Stive (1989), Bar-generating cross-shore flow mechanisms on a beach, Journal of Geophysical Research: Oceans, 94(C4), 4785-4800, doi:10.1029/JC094iC04p04785.

Ruessink, B. G., H. Michallet, P. Bonneton, D. Mouaze, J. Lara, P. A. Silva, and P. Wellens (2013), Globex: wave dynamics on a gently sloping laboraty beach, paper presented at 7th International Conference on Coastal Dynamics.

Sheremet, A., J. M. Kaihatu, S. F. Su, E. R. Smith, and J. M. Smith (2011), Modeling of nonlinear wave propagation over fringing reefs, Coastal Engineering, 58(12), 1125-1137, doi:https://doi.org/10.1016/j.coastaleng.2011.06.007.

Smit, P., T. T. Janssen, L. Holthuijsen, and J. J. Smith (2014), Non-hydrostatic modeling of surf zone wave dynamics, Coastal Engineering, 83, 36-48, doi:10.1016/j.coastaleng.2013.09.005.

Thotagamuwage, D. T., and C. B. Pattiaratchi (2014a), Influence of offshore topography on infragravity period oscillations in Two Rocks Marina, Western Australia, Coastal Engineering, 91(91), 220-230.

Thotagamuwage, D. T., and C. B. Pattiaratchi (2014b), Observations of infragravity period oscillations in a small marina, Ocean Engineering, 88, 435-445, doi:https://doi.org/10.1016/j.oceaneng.2014.07.003.

Tucker, M. (1950), Surf Beats: Sea Waves of 1 to 5 Min. Period, Proceedings of the Royal Society A, 202(1071), 565-573.

Van Dongeren, A., H. J. Bakkenes, and T. T. Janssen (2002), Generation of long waves by short wave groups, in Coastal Engineering 2002, edited, pp. 1093-1105, doi:10.1142/9789812791306_0093.

Van Dongeren, A., J. A. Battjes, T. T. Janssen, J. V. Noorloos, K. Steenhauer, G. Steenbergen, and A. Reniers (2007), Shoaling and shoreline dissipation of low-frequency waves, Journal of Geophysical Research: Oceans, 112(C2), doi:10.1029/2006JC003701.

Van Leeuwen, P. J. (1992), Low frequency wave generation due to breaking waves, Ph.D dissertation thesis, Delft university of technology, Delft, Netherlands.

Shuto, N. (1974), Nonlinear Long Waves in a Channel of Variable Section, *Coastal Eng Japan*, *17*(1), 1-12.

Wang, B., A. J. Chadwick, and A. K. Otta (2008), Derivation and application of new equations for radiation stress and volume flux, *Coastal Engineering*, *55*(4), 302-318, doi:https://doi.org/10.1016/j.coastaleng.2007.11.008.

Zijlema, M., G. Stelling, and P. Smit (2011), SWASH: An operational public domain code for simulating wave fields and rapidly varied flows in coastal waters, Coastal Engineering, 58(10), 992-1012, doi:10.1016/j.coastaleng.2011.05.015.

Zou, Q. (2011), Generation, Transformation, and Scattering of Long Waves Induced by a Short-Wave Group over Finite Topography, Journal of Physical Oceanography, 41(10), 1842-1859, doi:10.1175/2011jpo4511.1.

Table 1. Slope conditions of the numerical tests

Run ID	Slope	x_1 (m)	x_4 (m)
1	1/100	15	145
2	1/80	26	134
3	1/60	37	123
4	1/40	48	112

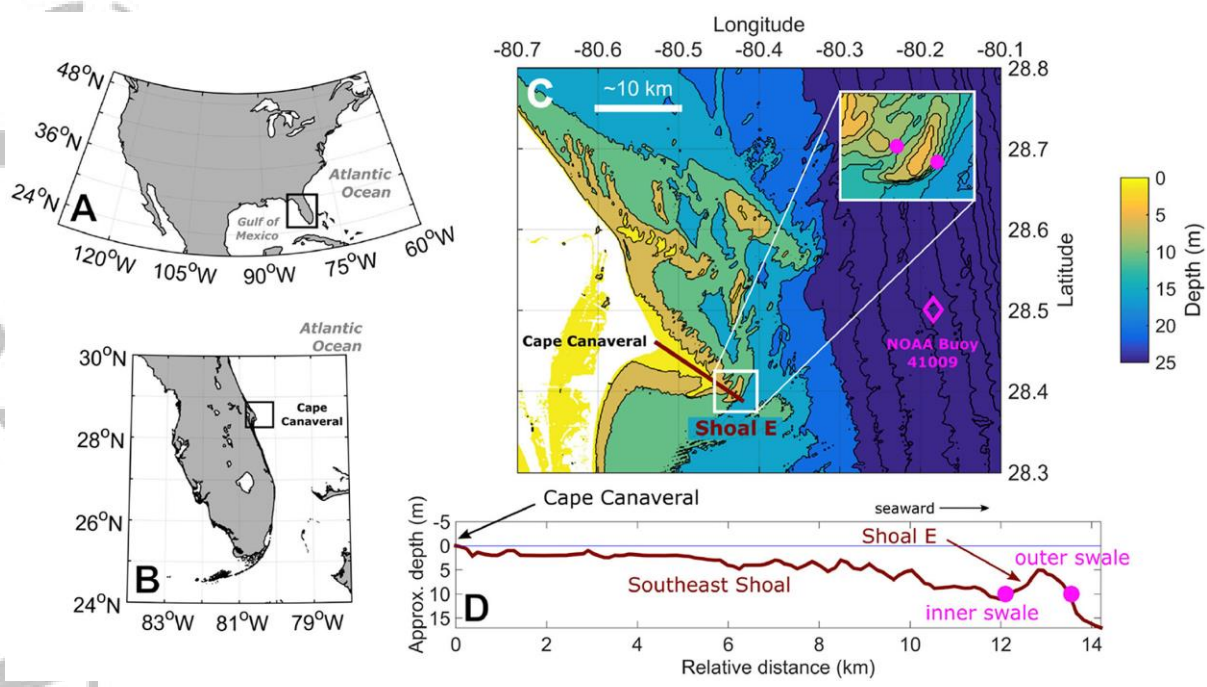

Figure 1. Location of acoustic Doppler current profilers (ADCPs) at Cape Canaveral shoals in *Paniagua-Arroyave et al.* [2019]. Magenta filled circles represent the approximate ADCP locations at the outer and inner swales of Shoal E (water depths 13 m). Black rectangles in A and B show the location of the Florida Peninsula within North America and Cape Canaveral on the Florida Peninsula, respectively. The map in C shows the inner shelf bathymetry near Cape Canaveral with an inset highlighting Shoal E. The brown line corresponds to an approximate bottom profile across Southeast shoal and Shoal E (D).

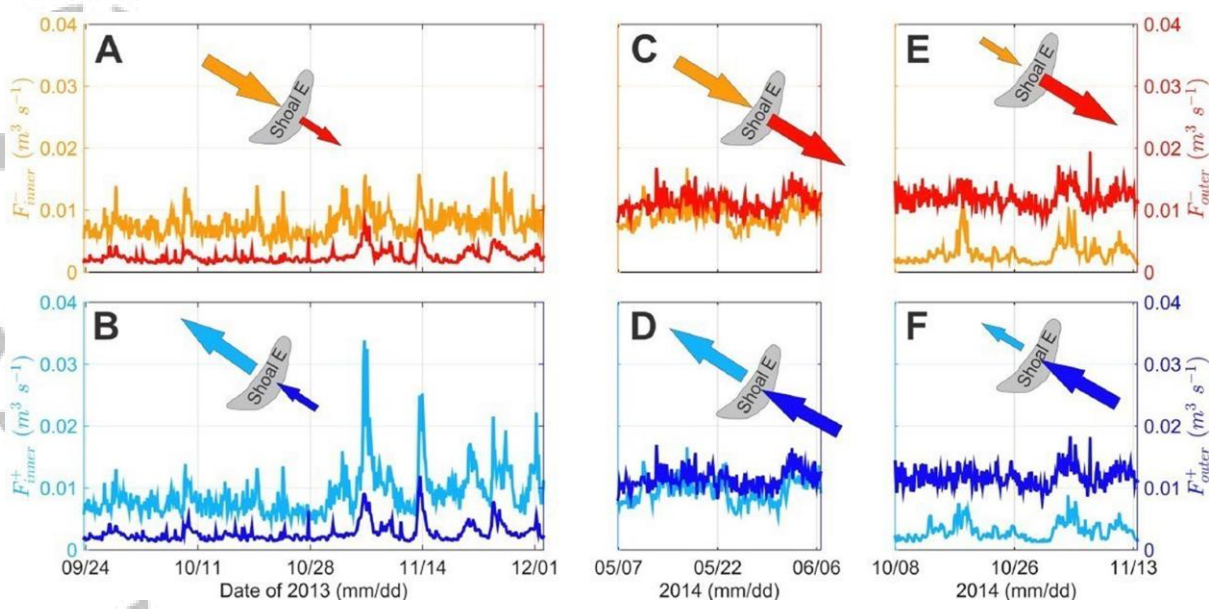

Figure 2**.** (A–F) Time series plots of seaward- (F^-) and landward-directed (F^+) cross-shoal IGW energy fluxes for inner (orange and turquoise lines) and outer (red and blue lines) swales in *Paniagua-Arroyave et al.* [2019]. During Fall 2013 (A and B) and Spring 2014 (C and D), the main direction of the SWs, $D_{p,}$ is shoreward perpendicular to the shoal; during Fall 2014 (E and F), $D_{p,}$ is seaward perpendicular to the shoal.

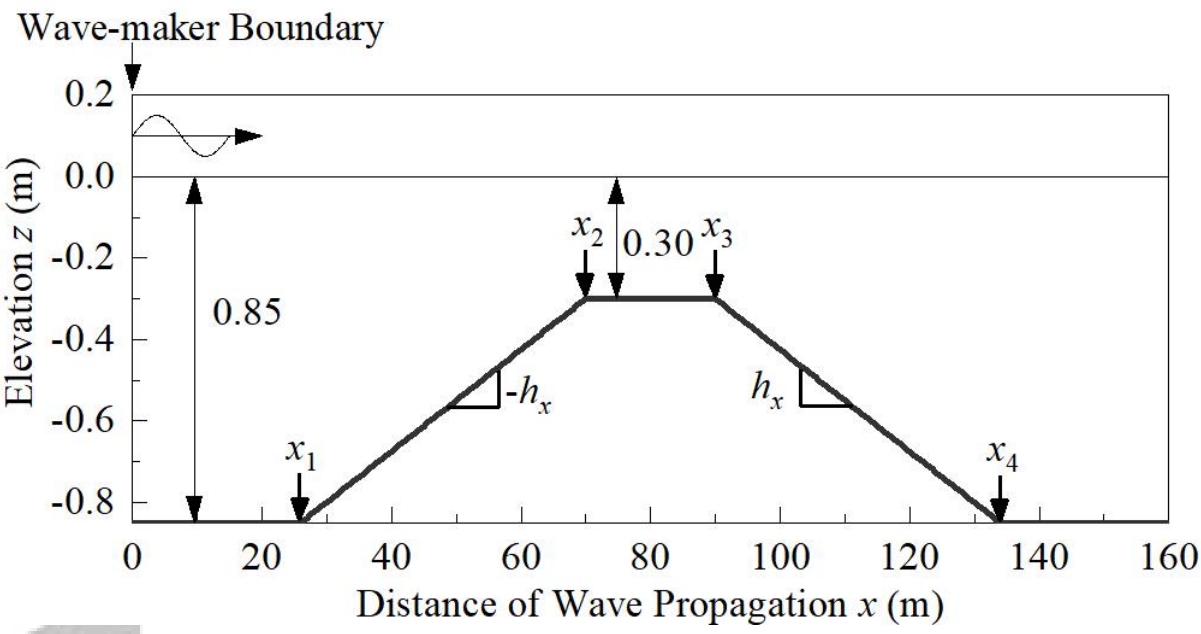

Figure 3. Sketch of idealized shoals in all runs of test. The original of the x coordinate was fixed at the wave-maker boundary. x_1 and x_4 are different for different test runs depending on the bottom slope; x_2 and x_3 are fixed to 70 m and 90 m, respectively.

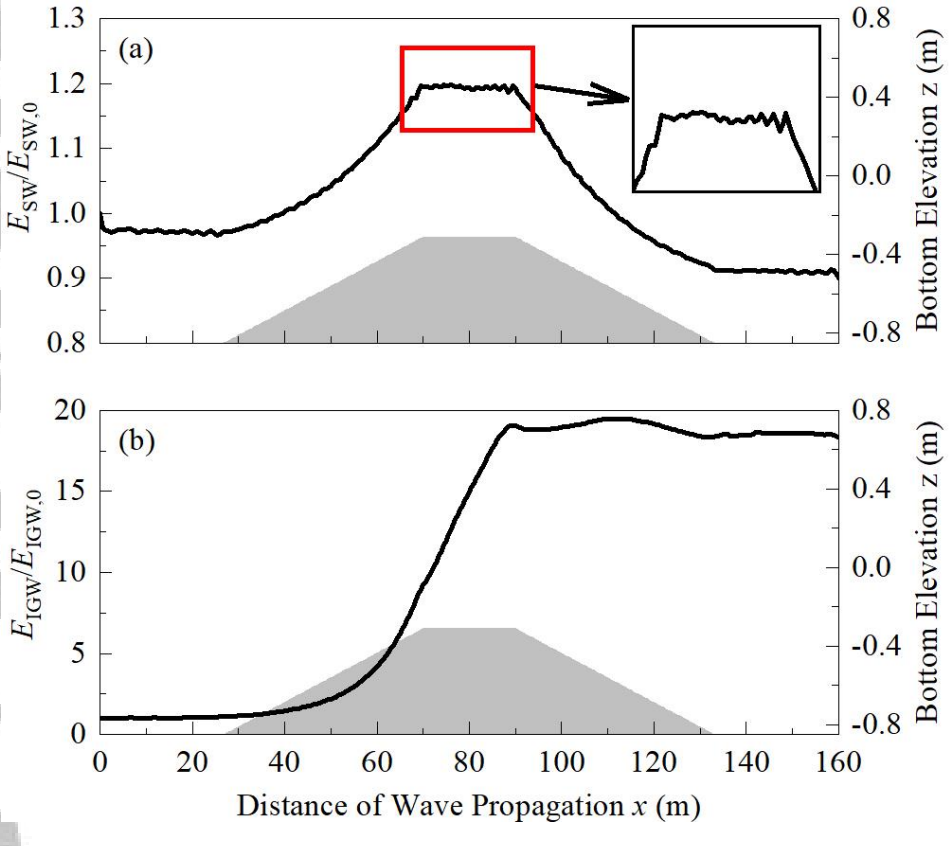

Figure 1. Spatial evolutions of normalized wave energy for Run 2 (bottom slope 1/80). (a) SW, and (b) IGW. The subscript 0 denotes quantities at the incident boundary.

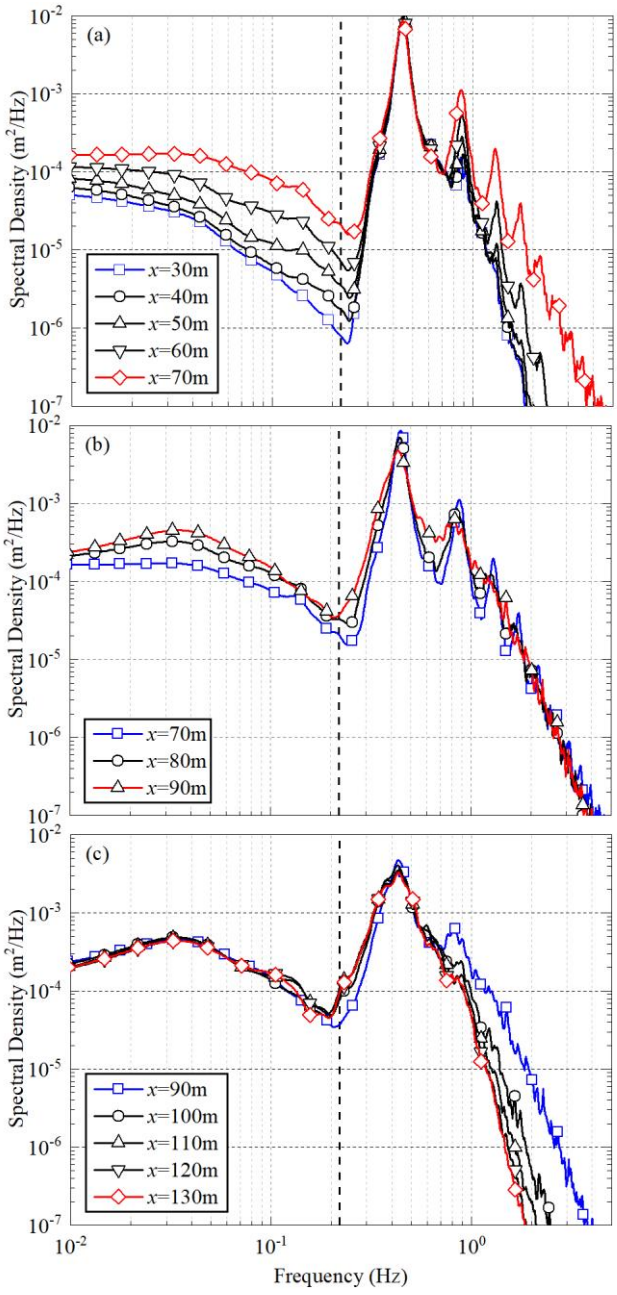

Figure 2. Wave spectra at different locations across the shoal for Run 2 (bottom slope 1/80). (a) front slope, (b) plateau, and (c) rear slope. The critical frequency between IGWs and SWs (0.22 Hz) is indicated by the vertical dash lines.

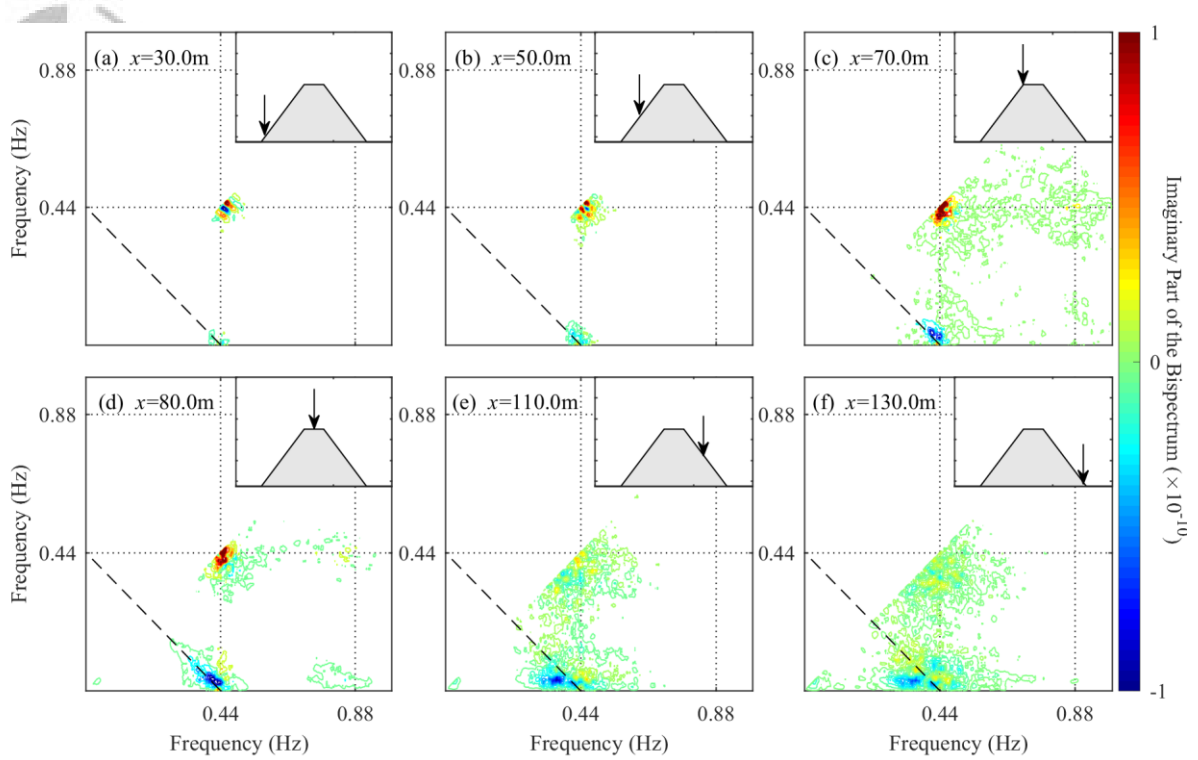

Figure 3. Imaginary parts of the wave bispectra at different positions across the shoal, Run 2 (bottom slope 1/80). (a) x = 30.0 m, (b) x = 50.0 m, (c) x = 70.0 m, (d) x = 80.0 m, (e) x = 110.0 m and (f) x = 130.0 m. The dash line in each subfigure indicates frequency pairs of which the sum is 0.44 Hz.

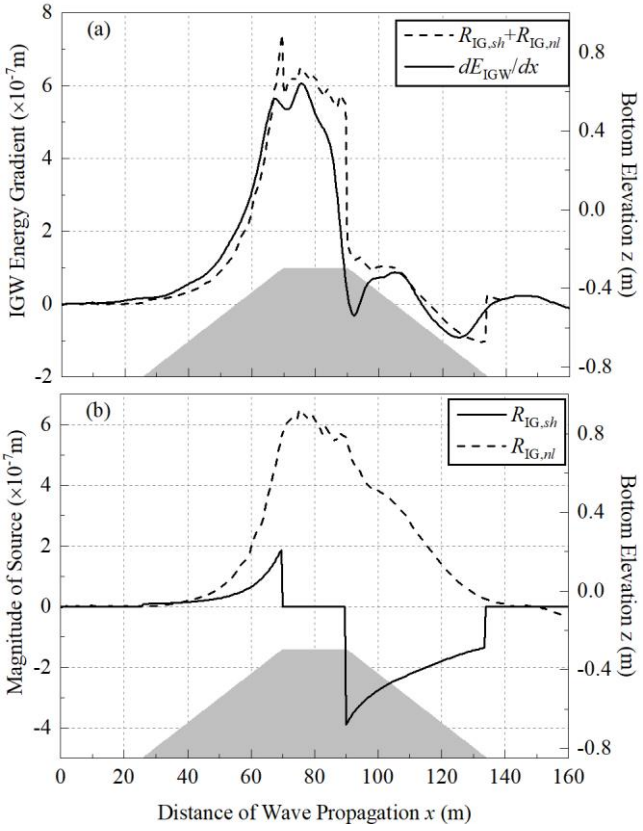

Figure 4. Spatial evolutions of (a) sum of the two source terms ($R_{IG,sh}$+ $R_{IG,nl}$) and gradient of IGW energy E_{IGW} from numerical simulation, (b) source terms of IGW energy E_{IGW} due to shoaling ($R_{IG,sh}$) and nonlinear interactions ($R_{IG,nl}$) of Run 2 (bottom slope 1/80).

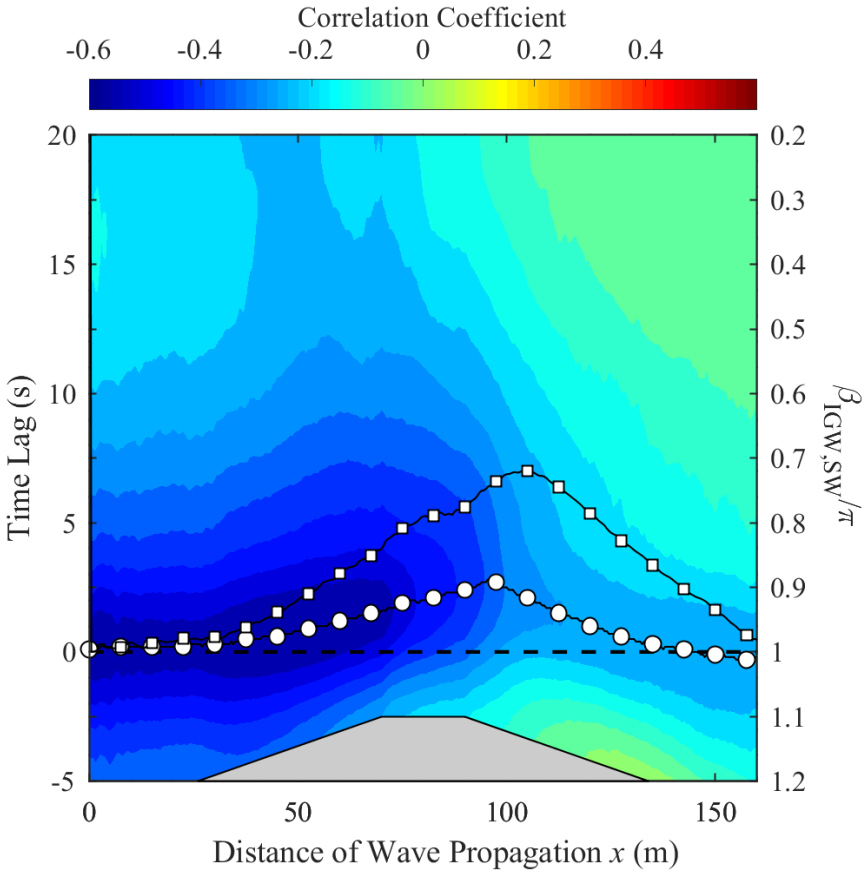

Figure 5. Cross-correlation between local surface elevations of IGWs and wave height history, Run 2 (bottom slope 1/80). The circled line indicates time lags of the minimal correlation coefficients and the squared line indicates the spatial evolution of the biphase $\beta_{IGW,SW}$. The gray trapezoid is a sketch of the topography.

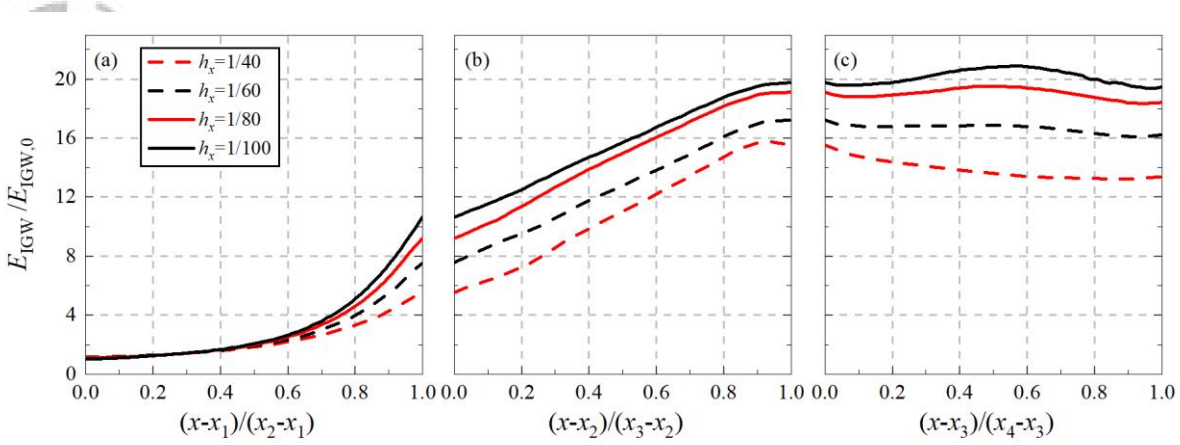

Figure 6. Spatial evolutions of the IGW energy for all runs of test with different slopes. (a) On the front slope, (b) On the plateau, (c) On the rear slope. Meanings of x_1 to x_4 are the same in

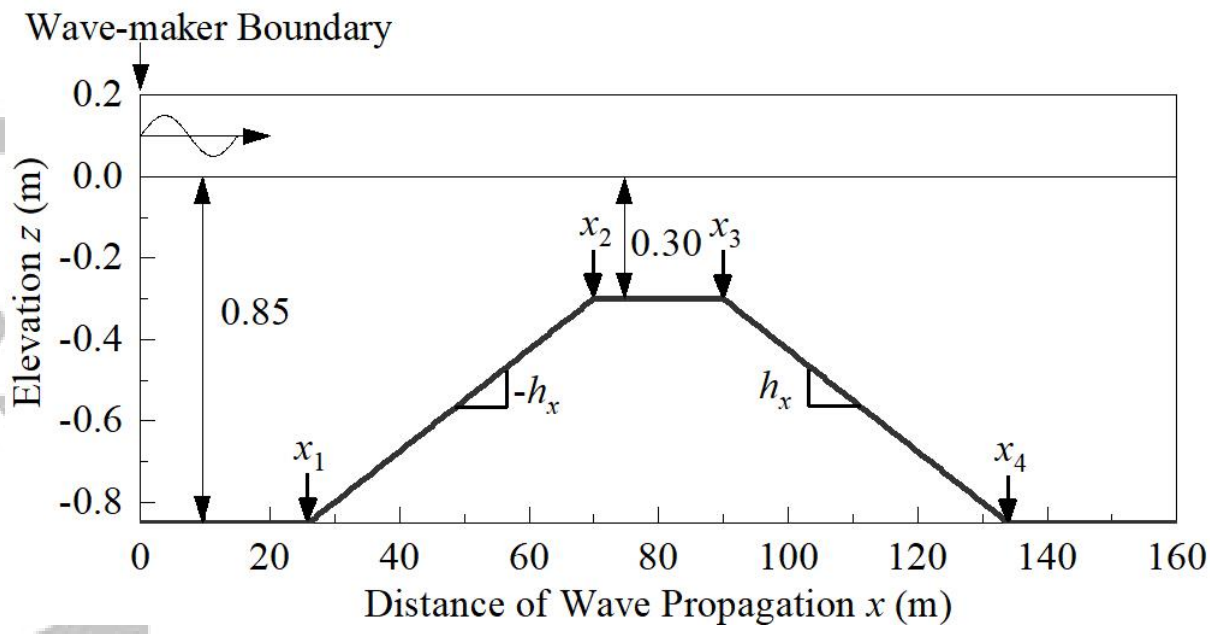

Figure.

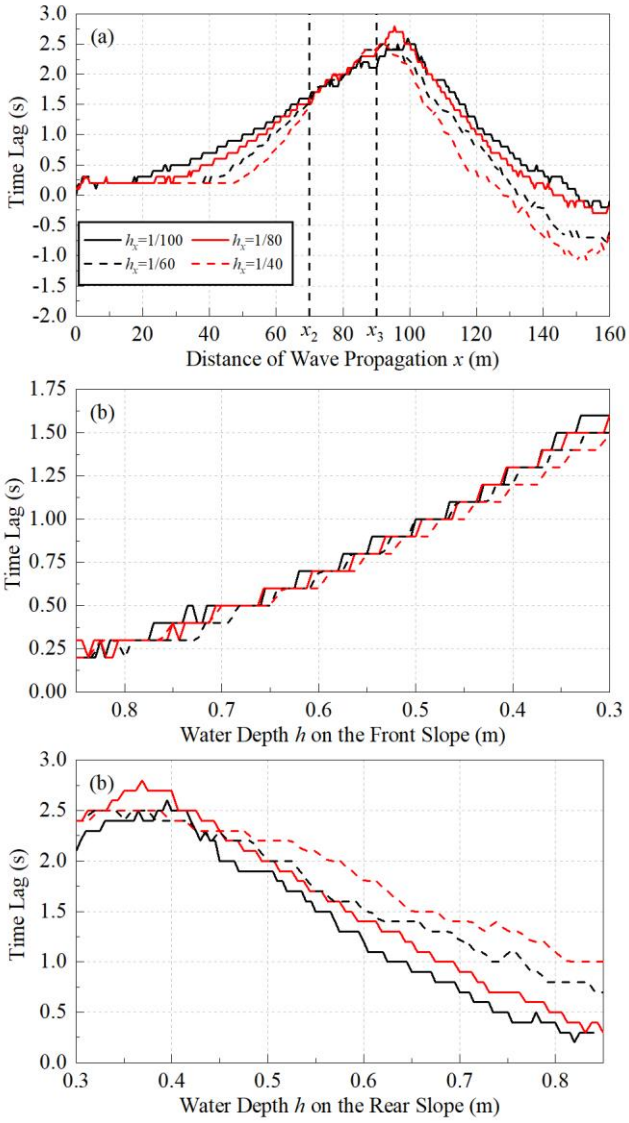

Figure 7. Spatial evolutions of the time lag between local IGWs and *WHH* for all runs of test. (a) Across the whole shoal with respect to horizontal coordinates *x*, (b) On the front slope with respect to local depth *h*, (c) On the rear slope with respect to local depth *h*.

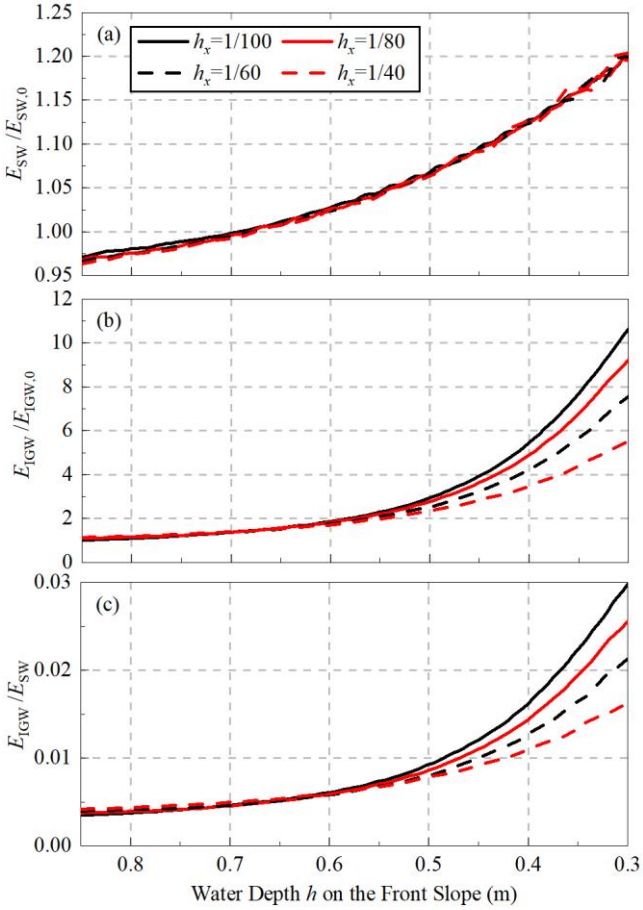

Figure 8. Evolution of wave energy with respect to local depth *h* on the front slope with different slopes. (a) SWs, (b) IGWs, (c) local energy ratio between IGW and SW.

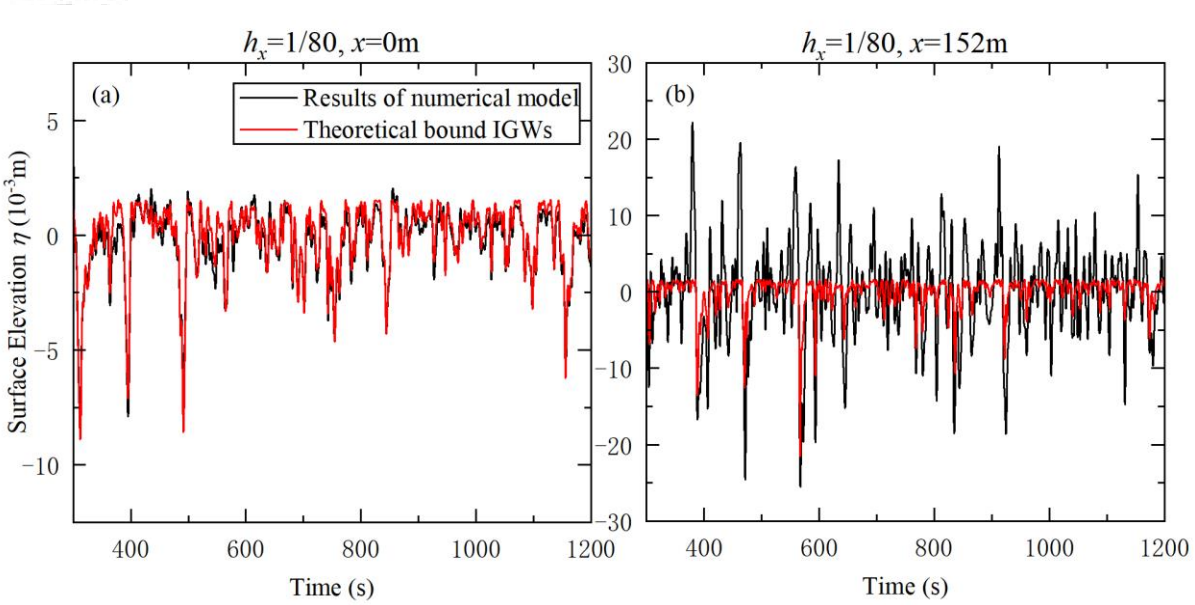

Figure 9. Comparison between SWASH model simulated IGWs and predicted bound IGWs by Eq. (A19) at (a) the incident boundary (x=0 m), and (b) the leeside of the shoal (x=152 m), Run 2 (bottom slope 1/80).

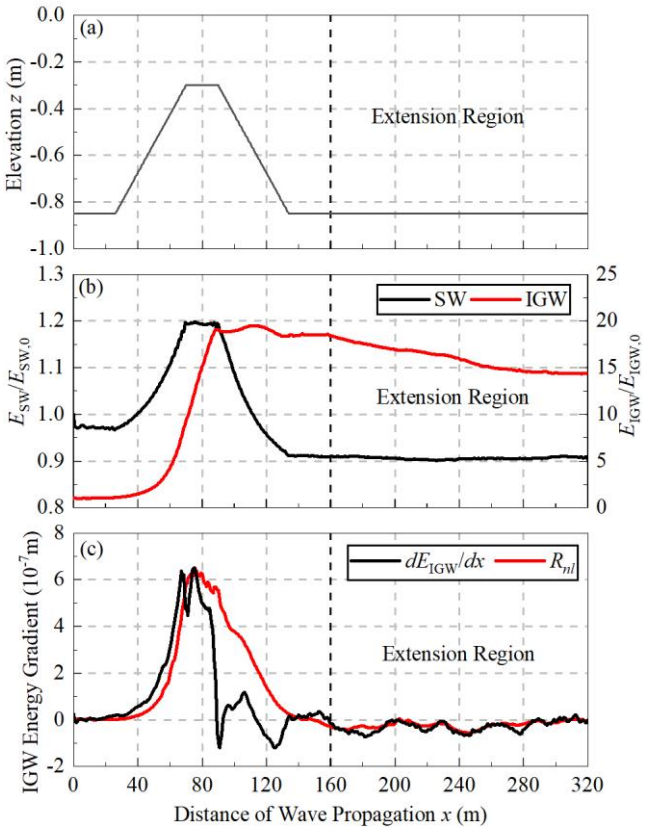

Figure 10. (a) Bathymetry modified from Run 2 (bottom slope 1/80) with the bottom extended additionally by 160 m, (b) Evolution of the normalized SW and IGW energy, (c) Evolution of the IGW energy gradient and nonlinear source term R_{nl}. The dash line indicates the position separating the original and extended flume.

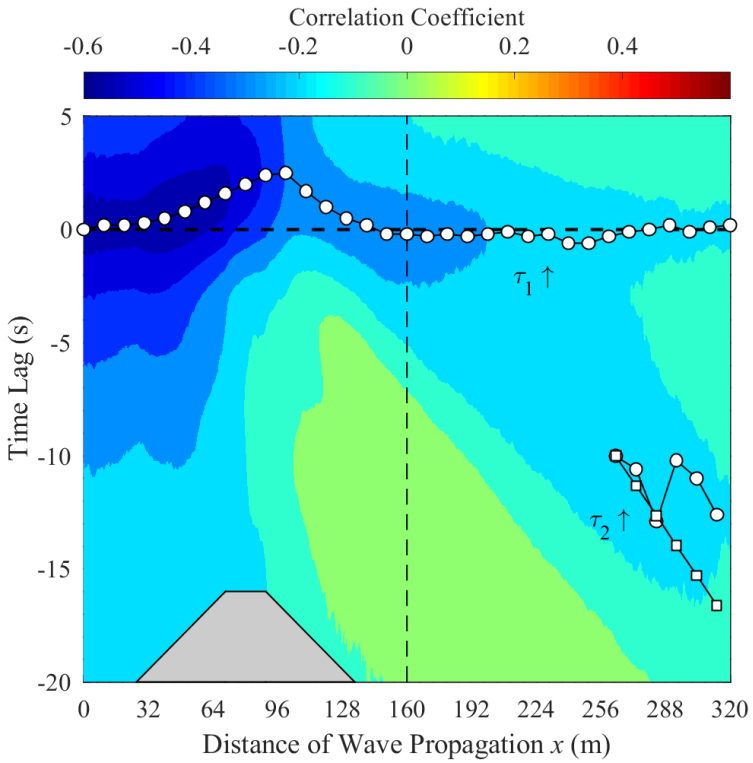

Figure 11. Cross-correlation between local surface elevation of IGWs and wave height history for Run 2 (bottom slope 1/80) with the flume extended 160 m longer. The circled line denotes time lags of the local minima of the cross-correlation function; the squared line is calculated with the free long wave speed and group speed evaluated with linear theory; the horizontal dash line separates the domain of Run 2 and the extended region. The gray trapezoid is a sketch of the topography.

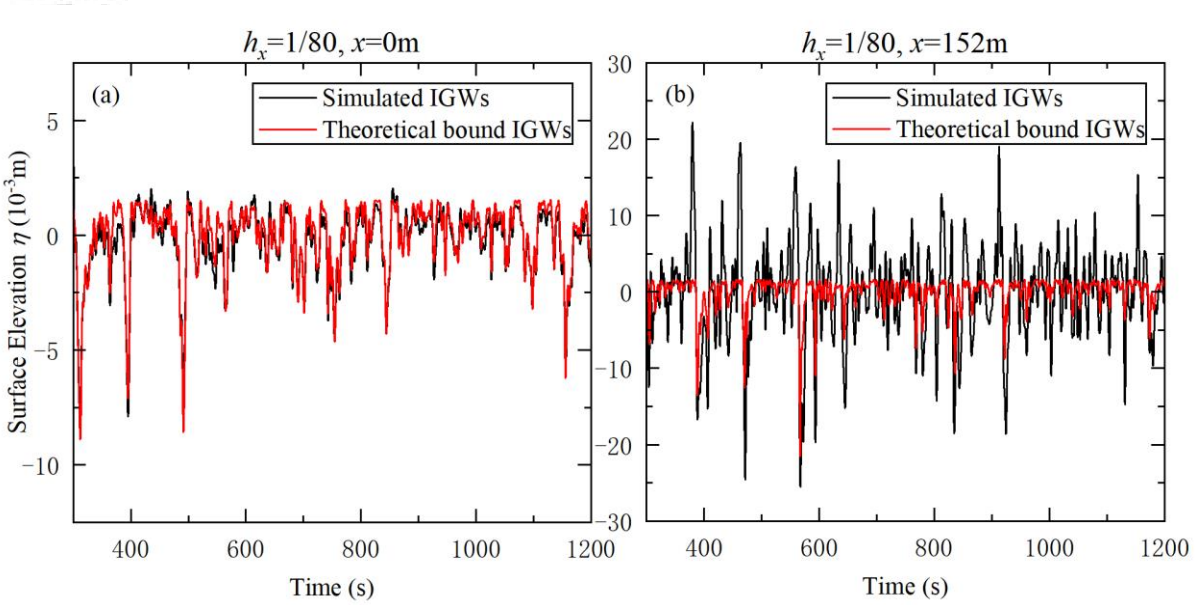

Figure 12. Free IGW energy relative to the incident IGW energy at leeward of the shoal for all test runs of different front and rear slopes.